

See discussions, stats, and author profiles for this publication at: <https://www.researchgate.net/publication/270823599>

Strong Electron Hybridization and Fermi-to-Non-Fermi Liquid Transition in $\text{LaCu}_3\text{Ir}_4\text{O}_{12}$

ARTICLE in CHEMISTRY OF MATERIALS · DECEMBER 2014

Impact Factor: 8.35 · DOI: 10.1021/cm503781s

CITATION

1

READS

93

11 AUTHORS, INCLUDING:



Manrong Li

Rutgers, The State University of New Jersey

76 PUBLICATIONS 493 CITATIONS

SEE PROFILE



Maria Retuerto

Rutgers, The State University of New Jersey

84 PUBLICATIONS 399 CITATIONS

SEE PROFILE



M. Croft

Rutgers, The State University of New Jersey

334 PUBLICATIONS 5,538 CITATIONS

SEE PROFILE



Martha Greenblatt

Rutgers, The State University of New Jersey

222 PUBLICATIONS 3,103 CITATIONS

SEE PROFILE

Strong Electron Hybridization and Fermi-to-Non-Fermi Liquid Transition in $\text{LaCu}_3\text{Ir}_4\text{O}_{12}$

Man-Rong Li,[†] Maria Retuerto,[†] Zheng Deng,[†] Tapati Sarkar,[†] Javier Sánchez-Benítez,[‡] Mark C. Croft,[§] Tanusri Saha Dasgupta,^{||} Tilak Das,^{||} Trevor A. Tyson,[⊥] David Walker,[#] and Martha Greenblatt^{*,†}

[†]Department of Chemistry and Chemical Biology, Rutgers, The State University of New Jersey, 610 Taylor Road, Piscataway, New Jersey 08854, United States

[‡]Departamento de Química Física I, Facultad de Ciencias Químicas, Universidad Complutense de Madrid, E-28040 Madrid, Spain

[§]Department of Physics and Astronomy, Rutgers, The State University of New Jersey, 136 Frelinghuysen Road, Piscataway, New Jersey 08854, United States

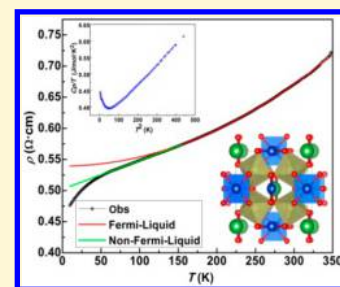
^{||}Department of Condensed Matter Physics and Materials Sciences, S. N. Bose National Centre for Basic Sciences, JD Block, Sector III, Salt Lake, Kolkata 700098, India

[⊥]Physics Department, New Jersey Institute of Technology, Newark, New Jersey 07102, United States

[#]Lamont-Doherty Earth Observatory, Columbia University, 61 Route 9W-PO Box 1000, Palisades, New York 10964, United States

S Supporting Information

ABSTRACT: The $\text{AA}'_3\text{B}_4\text{O}_{12}$ -type quadruple perovskite $\text{LaCu}_3\text{Ir}_4\text{O}_{12}$ prepared at high pressure (9 GPa) and temperature (1523 K) crystallizes in cubic symmetry ($Im\bar{3}$, $a = 7.52418(3)$ Å) with square planar CuO_4 and octahedral IrO_6 coordination as established from synchrotron powder X-ray diffraction studies. Both crystal structure and X-ray absorption near edge spectroscopy analyses indicate formal oxidation states of $\text{LaCu}^{2+}_3\text{Ir}^{3.75+}_4\text{O}_{12}$. The temperature dependence of resistivity of $\text{LaCu}_3\text{Ir}_4\text{O}_{12}$ is metallic down to 10 K, with Fermi-liquid behavior above $T^* \sim 155$ K, and non-Fermi-liquid behavior below T^* . The two-fluid behavior of magnetic susceptibility and the dramatic downturn of the resistivity below T^* indicate strong Cu^{2+} 3d and $\text{Ir}^{3.75+}$ 5d orbital hybridization below T^* , also supported by an enhanced electronic specific heat coefficient at low temperature. Theoretical calculations are in good agreement with the experimental results and show that the electronic structure of $\text{LaCu}_3\text{Ir}_4\text{O}_{12}$ is different from that of $\text{CaCu}^{2+}_3\text{Ir}^{4+}_4\text{O}_{12}$, which is also metallic down to 0.5 K, but presents non-Fermi liquid behavior above $T^* \sim 80$ K and strong Cu-3d–Ir-5d orbital coupling at significantly lower temperature ($T < T^* \sim 80$ K).



1. INTRODUCTION

ABO_3 perovskites continue to attract much research, because of their wide variety of important physical properties such as superconductivity, ferroelectricity, magnetoresistance, and multiferroic behavior.^{1–4} Interest in the quadruple perovskites $\text{AA}'_3\text{B}_4\text{O}_{12}$ (A = mono- or divalent cations or rare earths; A' = Jahn–Teller (JT) cations; B = transition metals) has been renewed due to the low-field magnetoresistance properties in $\text{ACu}_3\text{Mn}_4\text{O}_{12}$,⁵ the giant dielectric constant of $\text{CaCu}_3\text{Ti}_4\text{O}_{12}$,⁶ the heavy Fermion behavior of $\text{CaCu}_3\text{Ru}_4\text{O}_{12}$,⁷ the magneto-electric properties of $\text{BiMn}_3\text{Mn}_4\text{O}_{12}$,⁸ and the charge transfer in $\text{LaCu}_3\text{Fe}_4\text{O}_{12}$.⁹ The crystal symmetry of $\text{AA}'_3\text{B}_4\text{O}_{12}$ perovskite-like phases is cubic (space group $Im\bar{3}$) with a doubling of the ideal perovskite cell, due to the ordering of the A and A' ions and the distortion of the oxygen sublattice, which leads to a tilted three-dimensional (3D) network of corner-sharing BO_6 octahedra. The B–O–B angle is $\sim 142^\circ$ instead of 180° , as in the ideal perovskite. This large distortion of the 3D network is due to the ordering of the A and A' cations, with two different coordination polyhedra: a slightly distorted 12 oxygen-coordinated A site and a highly distorted A' site of a nearly square-planar coordination. The $\text{AA}'_3\text{B}_4\text{O}_{12}$ is mostly stable

with $\text{A}' = \text{Cu}^{2+}$ (d^9) or Mn^{3+} (d^4), both JT distorted ions. Very recently $\text{CaPd}_3\text{B}_4\text{O}_{12}$ (B = Ti and V) was reported with Pd^{2+} (d^8 , low spin) square planar coordination.¹⁰ Typically, a high pressure synthesis technique is required to stabilize the $\text{AA}'_3\text{B}_4\text{O}_{12}$ perovskite.

In the recent past, much attention has been focused on the chemistry of oxides containing 4d and 5d transition metal cations, since they exhibit interesting electronic and magnetic properties.¹¹ The increased spatial extent of 4d and 5d, compared to the more localized 3d orbitals of the first row transition metals, yields a weaker on-site Coulomb interaction and a greater level of splitting in the crystal field, increasing their sensitivity to lattice distortions, especially in layered oxides such as Sr_2RuO_4 , Sr_2RhO_4 , Sr_2IrO_4 , and Na_2IrO_3 .^{12–14} Moreover, the energy of the spin–orbit coupling approaches that of the on-site Coulomb interactions modifying the relative energy scale and showing up unusual electronic structures.¹⁵ Iridium can form oxides in different oxidation states, and its

Received: October 15, 2014

Revised: December 11, 2014

Published: December 15, 2014

extended 5d orbitals together with spin–orbit coupling (SOC) can lead to a rich variety of interesting properties.

Recently, Cheng et al.^{16,17} prepared the first Ir containing quadruple perovskite, $\text{CaCu}_3\text{Ir}_4\text{O}_{12}$ (CCIO) at 9 GPa, which showed linear- T metallic behavior above T^* at ~ 80 K, followed by a strong downward trend down to 0.5 K in the resistivity. The low-temperature ($T < T^*$) specific heat, magnetic susceptibility, and thermoelectric power show non-Fermi-liquid behavior suggestive of nearby quantum critical behavior. CCIO presents a large electronic specific-heat coefficient, γ , with no magnetic ordering down to 0.35 K, and a magnetic contribution emerging at low temperature, which suggests a magnetic quantum critical point. The anomalous physical properties of CCIO suggest Kondo behavior of Cu^{2+} moments coupled to Ir d orbitals that are close to a metal–insulator crossover.¹⁷ In this work we focused on the La analogue of CCIO, $\text{LaCu}_3\text{Ir}_4\text{O}_{12}$ (LCIO), with Ir in a formally mixed-valent oxidation state ($\text{LaCu}_3[\text{Ir}^{4+}_3\text{Ir}^{3+}]_4\text{O}_{12}$), which was synthesized under high pressure and temperature (HPT). Here we present the chemical and physical properties of LCIO and show that LCIO-like CCIO is metallic down to low temperature; however, it differs from CCIO in that it undergoes a non-Fermi-to-Fermi liquid behavior above $T^* \sim 155$ K. The susceptibility, resistivity, and specific heat of LCIO evidence strong orbital hybridization of Cu^{2+} -3d and $\text{Ir}^{3+/4+}$ -5d electrons below T^* .

2. EXPERIMENTAL SECTION

Synthesis. A stoichiometric mixture of La_2O_3 (99.99% Alfa Aesar, preheated at 1273 K in air overnight), CuO (99.99% Sigma-Aldrich), Ir powder (99.9%, Alfa Aesar), and IrO_2 (99.99% Alfa Aesar) was reacted at 1523 K under 9 GPa pressure for 1 h in a LaCrO_3 heater lined with Pt capsule inside a MgO crucible in a multianvil press¹⁸ and then quenched to room temperature (RT) by turning off the voltage supply to the resistance furnace. The pressure was maintained during the temperature quenching and then released slowly in 8–12 h.

X-ray Diffraction, Absorption Fine-Structure, and Near Edge Absorption Spectroscopy. The product was initially characterized by laboratory powder X-ray diffraction (PXD, Bruker D8 ADVANCE, $\text{Cu K}\alpha$, $\lambda = 1.5406$ Å) for phase identification and purity. Synchrotron powder X-ray diffraction (SPXD, $\lambda = 0.779187$ Å, instrument resolution of 0.005°) data were collected at RT at the X14A beamline in the Brookhaven National Synchrotron Light Source (NSLS). Rietveld refinements of the SPXD data were carried out with TOPAS program package.^{19,20} X-ray absorption fine-structure (XAFS) data were collected at beamline X3A (NSLS) and X-ray near edge absorption spectroscopy (XANES) data at X11A (NSLS). Layers of powder brushed onto Kapton tape were stacked to produce a uniform sample for transmission measurements with jump $\mu t \sim 1$. Measurements were made on a sample attached to the coldfinger of a cryostat. Three-to-six scans were taken at each temperature. At the Cu and Ir L_3 edges, the corresponding metal foils were used for energy calibration. The reduction of the XAFS data was performed with standard procedures.²¹ For the Ir L_3 edge and Cu K edge data, the k -ranges $1.53 < k < 19.53$ Å⁻¹ and $2.34 < k < 18.36$ Å⁻¹ were used, respectively ($k = [(E - E_0)2m]^{1/2}/\hbar$ and the ionization energy is E_0) to obtain the Fourier transforms.

Magnetic and Resistivity Measurements. Magnetization measurements were carried out with a commercial Quantum Design superconducting quantum interference device (SQUID) magnetometer. The susceptibility was measured in field cooled (FC) and zero field cooled (ZFC) modes under a 0.1 T magnetic field, for temperatures ranging from $T = 5$ to 300 K. Transport and magnetotransport measurements were performed by the conventional four-probe technique in the temperature range 10–350 K in a Physical Property Measurements System (PPMS) from Quantum Design. Heat capacity measurements were conducted in a Quantum Design PPMS

system on warming and cooling over the range 2 to 390 K utilizing a relaxation method.²² A blank run (Apiezon grease without sample) was made and subtracted from the sample measurement. No significant evidence of hysteresis was observed.

First Principle Calculations. The theoretical calculations of the electronic structure of LCIO in comparison to CCIO were carried out with density functional theory (DFT) calculations in linear augmented plane wave basis.²³ The strong correlation effect at the transition metal sites was taken into account through GGA + U calculation, with the U value for the 3d transition metal, Cu chosen as 5 eV and that of 5d transition metal, Ir chosen as 2 eV, with Hund's energy (J_H) of 0.8 eV. The 5d Ir ions are known to produce fascinating physics driven by spin–orbit coupling.^{24–26} Calculations were therefore repeated with GGA + U + SO scheme.

3. RESULTS AND DISCUSSION

3.1. Crystal Structure. The PXD pattern of LCIO can be well indexed in a body-centered cubic unit cell, which is characteristic of a perovskite with well-defined superstructure reflections due to the La: Cu 1:3 ordering over the A and A' sites, respectively. The weak impurity peaks are identified to be IrO_2 . The structural refinement was performed on RT SPXD data based on the structural model of CCIO with cubic $Im\bar{3}$ (No. 204) space group. Figure 1 shows excellent agreement

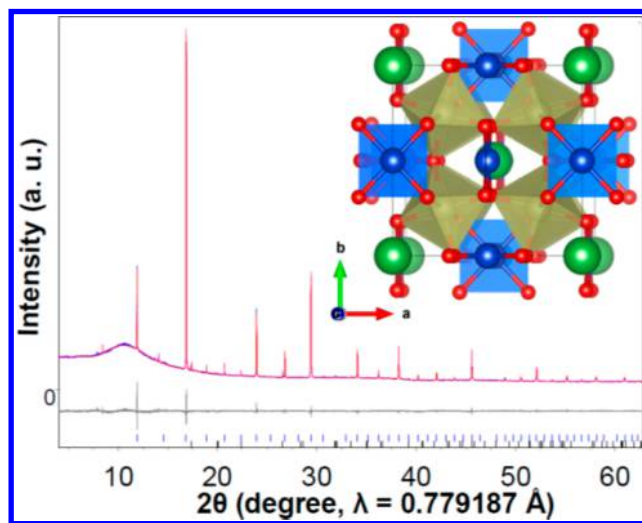


Figure 1. Experimental, calculated, and difference of the RT SPXD patterns of LCIO. Inset shows the unit cell crystal structure. La, green spheres; CuO_4 planes, blue; IrO_6 octahedra, tan; O, red spheres. Tick marks (l) indicate the index of LCIO (upper row) and IrO_2 impurity (bottom row) phases, respectively.

between the observed and calculated patterns ($R_p = 1.84\%$, $R_{wp} = 2.65\%$) and $\sim 3.8\%$ IrO_2 impurity. As observed in other similar materials, such as $\text{LaCu}_3\text{Cr}_4\text{O}_{12}$ and $\text{LaCu}_3\text{Mn}_4\text{O}_{12}$,^{27,28} the La atoms are located at $2a$ (0, 0, 0) positions, Cu at $6b$ (0, 1/2, 1/2), Ir at $8c$ (1/4, 1/4, 1/4), and O atoms at $24g$ ($x, y, 0$) in LCIO. Table 1 summarizes the refined structural parameters at RT and Table 2 the main bond distances and angles. The inset of Figure 1 shows a schematic view of the crystal structure. The unit-cell parameter of LCIO ($a = 7.52418(3)$ Å at RT) is twice the size of the simple perovskite and slightly larger than that of CCIO ($7.47380(6)$ Å),¹⁷ which is consistent with the slightly larger size of La^{3+} (1.03 Å) than Ca^{2+} (1.00 Å), in 12-coordination;²⁹ and also, considering the charge balance (required nominal $\text{Ir}^{3.75+}$ in LCIO) with the presence of some Ir^{3+} (0.68 Å), which is larger than the all Ir^{4+} (0.625 Å) in

Table 1. Comparison of the Structure Parameters of LCIO and CCIO at RT (space group $Im\bar{3}$ (No. 204), $Z = 2$)

	A = La	A = Ca
a , Å	7.524183(3)	7.47380(6)
V , Å ³	425.97(1)	417.47(1)
A (2a, 0 0 0)		
B_{iso} , Å ²	0.58(8)	0.37(7)
MM, μ_B	−0.01	−0.01
Cu (6b, 0 1/2 1/2)		
B_{iso} , Å ²	0.76(6)	0.90(2)
MM, μ_B	0.65	0.65
Ir (8c, 1/4 1/4 1/4)		
B_{iso} , Å ²	0.72(1)	0.30(1)
MM, μ_B	0.54	0.70
O (24g, x y 0)		
x	0.306(1)	0.3040(1)
y	0.178(1)	0.1719(10)
B_{iso} , Å ²	1.0(2)	0.04(4)
MM, μ_B	0.15	0.17

Table 2. Comparison of Selected Interatomic Distances (Å), Bond Valence Sums (BVS), and Bond Angles (deg) in LCIO and CCIO at RT

	A = La	A = Ca
bond lengths		
A–O (×12)	2.665(11)	2.610(7)
Cu–O (×4)	1.980(11)	1.948(8)
Cu–O (×4)	2.828(11)	2.856(4)
Ir–O (×6)	2.003(4)	1.999(3)
bond angles		
O–Cu–O	84.9(5)	82.5(5)
O–Ir–O	90.1(4)	88.6(3)
Ir–O–Ir	139.9(0)	138.4(1)
Cu–O–Ir	109.7(3)	110.1(2)

CCIO.²⁹ In addition, considering the cell parameter of $LaCu_3Mn_4O_{12}$ ($a = 7.3272(4)$ Å),²⁸ the replacement of Mn^{4+}/Mn^{3+} ($0.53/0.64$ Å)²⁹ by Ir^{4+}/Ir^{3+} cations will increase the B–O distances, expanding the unit cell of LCIO.

La^{3+} exhibits a regular dodecahedral environment, with 12 equal La–O distances (2.665(11) Å) at RT. However, the Cu^{2+} oxygen environment is highly distorted with four very long Cu–O distances (2.828(11) Å) and an effective coordination number of four with a pseudosquare planar environment of Cu–O bond lengths of 1.980(11) Å, consistent with JT Cu^{2+} . These CuO_4 units are not strictly coplanar since the values of O–Cu–O angles are $\sim 87^\circ$. The Ir^{4+}/Ir^{3+} cations are at the center of corner-sharing IrO_6 octahedra with all Ir–O bond lengths of 2.003(4) Å. The Ir–O–Ir bond angles are $\sim 140^\circ$, far away from 180° of the ideal cubic perovskite. The strong distortion of the structure occurs due to the small size of La and Cu cations forcing the Ir octahedra to tilt in order to optimize the A–O distances. Bond valence sums (BVS) calculations³⁰ (Table 2) yield formal oxidation states of $Cu^{1.97+}$, $Ir^{4.21+}$ in LCIO, which are $Cu^{2.11+}$ and $Ir^{4.23+}$ in CCIO.¹⁷ The BVS values of Ir are somewhat higher than the nominal values in LCIO ($Ir^{3.75+}$) and CCIO (Ir^{4+}), indicating electron delocalization and covalent component of the bonds.

3.2. XAFS and XANES. XAFS data (Figure 2) were collected up to ~ 20 Å^{−1} at both the Ir L_3 edge and the Cu K edge to probe the local structure about Ir and Cu, respectively.

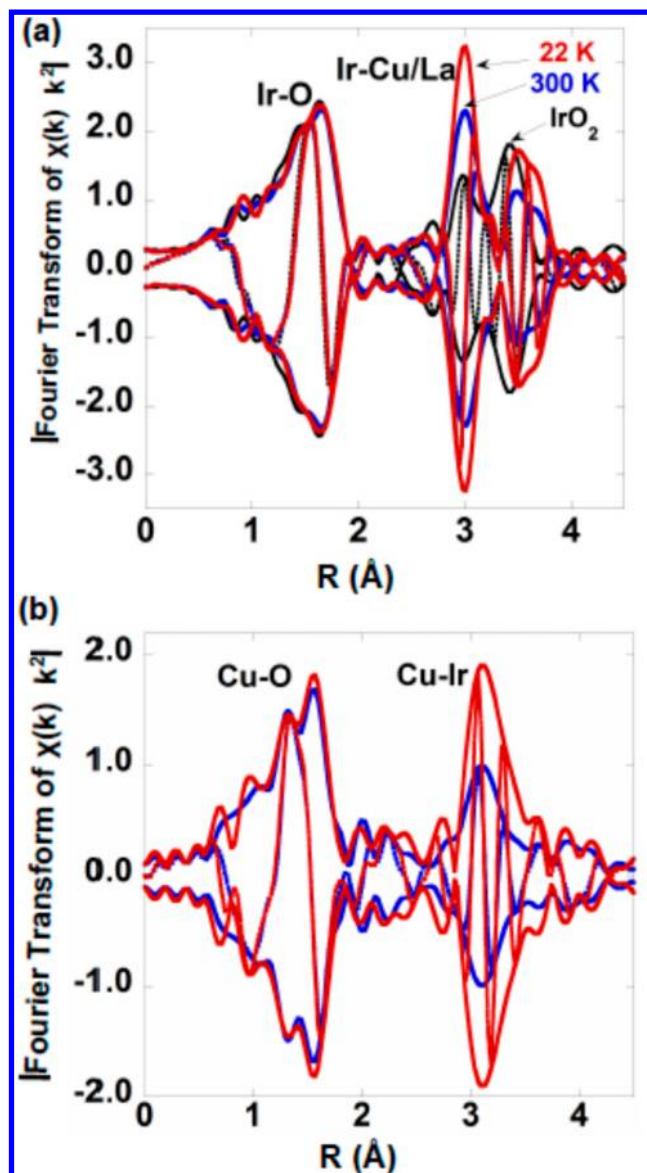


Figure 2. (a) Structure function (Fourier transform of the Ir L_3 XAFS fine structure) of LCIO at 300 and 22 K about the Ir site compared to IrO_2 at 300 K. Note that the amplitude and position of the first Ir–O nearest neighbor peak of LCIO does not change significantly with temperature indicating extremely stiff Ir–O bonds in this material. The coordination in the IrO_6 polyhedra is similar to that of IrO_2 . (b) Structure function about the Cu site at 300 and 22 K shows the typical temperature dependence in the first shell (Cu–O here) seen in transition metal oxides.

By comparing the data collected at 300 and 22 K, it is found that while the Cu sites exhibit the typical temperature dependence of other transition metal oxides such as manganites,³¹ by contrast, the Ir polyhedra exhibit negligible temperature dependence and indicate that these systems possess extremely rigid IrO_6 octahedra. This rigid behavior of the polyhedra will support strong coupling between adjacent Ir sites.

XANES is a useful tool for locally probing the valence states at atomic sites in solids. The near edge features at the K edges of 3d row transition metal, $T(3d)$, compounds are due to transitions from the 1s to 4p states of the transition metal, combined with a step feature for the continuum onset. Multiple

4p features associated with different local ligand coordination, mixed 3d configurations, and differing orbital orientations, complicate near edge structure.^{31,32} Nevertheless the systematic energy shifts in the T(3d) K edges, doping/chemical changes can serve as indicators of charge transfer.^{32–38}

The Cu–K and Ir–L₃ near edges of LCIO (along with those of various standards) are presented in Figure 3. Both the

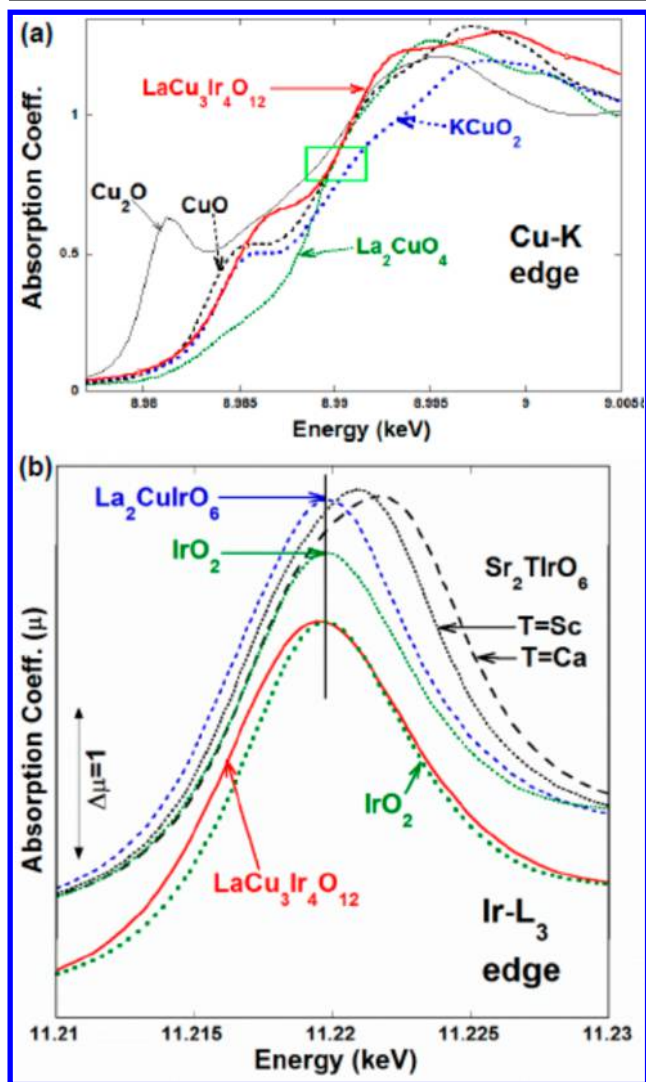


Figure 3. (a) Cu–K edge of $\text{LaCu}_3\text{Ir}_4\text{O}_{12}$ compared to those of standard compounds: Cu^{1+} , Cu_2O ; Cu^{2+} , CuO ; and formally Cu^{3+} , KCuO_2 . (b) The Ir–L₃ edges for a series of formal valence Ir-standard compounds: Ir^{6+} , $\text{Sr}_2\text{CaIrO}_6$; Ir^{5+} , $\text{Sr}_2\text{ScIrO}_6$; Ir^{4+} , IrO_2 and $\text{La}_2\text{CuIrO}_6$. A comparison of the Ir–L₃ edges of $\text{LaCu}_3\text{Ir}_4\text{O}_{12}$ and IrO_2 (scaled to equal peak intensity) is included with a vertical scale displacement for clarity.

structure and the chemical shifts of the near edge structure are sensitive to the valence and local atomic environment. Figure 3a compares the Cu–K edge of LCIO to those of a series of Cu compounds with varying formal valences and Cu–O coordination: Cu^{1+} , Cu_2O with linear 2-fold coordination;³⁹ Cu^{2+} , CuO with square planar coordination;⁴⁰ Cu^{2+} , La_2CuO_4 with distorted octahedral coordination;³⁰ and Cu^{3+} , KCuO_2 ⁴¹ with square planar coordination. It should be noted that in each of these cases the formal valences have been interpreted in terms of hybridized superpositions of differing *d*-configurations.

Indeed varying the formal Cu valence around 2+ typically involves strong covalency effects and subtle changes in the Cu–K edge best discerned by differential spectral comparisons.^{35,36} With such complications in mind the chemical shift of the LCIO spectrum (see green boxed region in figure) appears consistent with a formal Cu^{2+} state in this compound. As it will be seen below, this is in line with the Ir–L₃ edge results and the formal charge balance in the compound.

The L₃ edges of 5d transition metal compounds manifest very intense “white line” (WL) features due to dipole transitions into localized final d states. In an octahedral ligand field (LF) the *d*-states are split into lower, t_{2g} (6X degenerate), and a higher, e_g (4X), multiplets. In many high-hole (low-electron) count octahedral T-4d/5d compounds, separate t_{2g} and e_g related features can be discerned in their L₃ edge spectra.³⁵ This structure is best illustrated in Figure 3b by the prominent t_{2g} -related shoulder on the low energy side of the WL-feature of the $\text{Sr}_2\text{CaIrO}_6$ spectrum. Figure 3b (top spectra) also shows the Ir–L₃ edges of formal valence standard compounds: Ir^{6+} , $\text{Sr}_2\text{CaIrO}_6$; Ir^{5+} , $\text{Sr}_2\text{ScIrO}_6$; Ir^{4+} , IrO_2 ; and $\text{La}_2\text{CuIrO}_6$. With decreasing Ir valence (decreasing t_{2g} -hole count) two spectral changes occur: the shoulder t_{2g} feature decreases in intensity becoming less discernible and the centrum energy of the WL feature manifests a chemical shift to lower energy. In Figure 3b (bottom spectra) the Ir–L₃ edge of LCIO is compared to that of IrO_2 (scaled to equal peak intensity). The vertical line indicates the peak positions of IrO_2 and $\text{La}_2\text{CuIrO}_6$ standards and the LCIO spectrum can be seen to be slightly chemically shifted to low energy relative to these Ir^{4+} standards. With a formal Cu valence of 2+ the Ir valence would indeed be expected to be pulled somewhat lower than 4+ which is generally in line with the Ir–L₃ edge results.

3.3. Magnetic and Resistivity Properties. Figure 4a shows the ZFC magnetic susceptibility (χ) vs temperature (*T*) plot of $\text{LaCu}_3\text{Ir}_4\text{O}_{12}$ measured at 0.1 T. The FC plot overlaps with the ZFC data and thus it is not shown for clarity. The signal of the IrO_2 impurity has been subtracted according to the weight fraction from Rietveld refinement.⁴² No signature of magnetic ordering transition can be found in the whole temperature region of $\chi(T)$ or $1/\chi(T)$. Above a specific temperature T^* around 155 K, the data can be fitted to the Curie–Weiss (CW) law, while a deviation from CW law is clearly seen below 155 K. The effective moment (μ_{eff}) and paramagnetic temperature (θ) obtained from the fit are 5.55 $\mu_B/\text{f.u.}$ and –397.9 K, respectively. The experimental value of μ_{eff} is much larger than what is expected based on the contribution by three Cu^{2+} (3 $\mu_B/\text{f.u.}$), as $\text{Ir}^{4+}/\text{Ir}^{3+}$ are expected to be itinerant with negligible local moments.^{43,44} This deviation may be attributed to orbital contribution from Ir.

The $\chi(T)$ below T^* was fitted by a two fluid model for heavy Fermion materials.⁴⁵ In this scenario, the local Cu^{2+} 3d orbitals hybridize with the 5d conduction electrons of $\text{Ir}^{4+}/\text{Ir}^{3+}$ to reduce their entropy. The increased 3d–5d orbital interaction is also seen in the resistivity data in Figure 4b. The compound is metallic down to 10 K, while different types of electron correlations are observed in regions of $\rho(T)$ divided by T^* . Above T^* (155 K), $\rho(T)$ fits Fermi liquid behavior, perfectly described by $\rho(T) = \rho_0 + A \times T^2$, where $\rho_0 = 0.539 \, \Omega \cdot \text{cm}$ and $A = 1.46 \times 10^{-6} \, \Omega \cdot \text{cm} \cdot \text{K}^{-2}$. It should be noted that $\rho(T)$ of CCIO follows a linear non-Fermi-liquid behavior above its own characteristic temperature ($T^* \sim 80 \, \text{K}$), indicating that electron correlations of the normal state in LCIO and CCIO are fundamentally different. For LCIO below T^* , $\rho(T)$ shows two

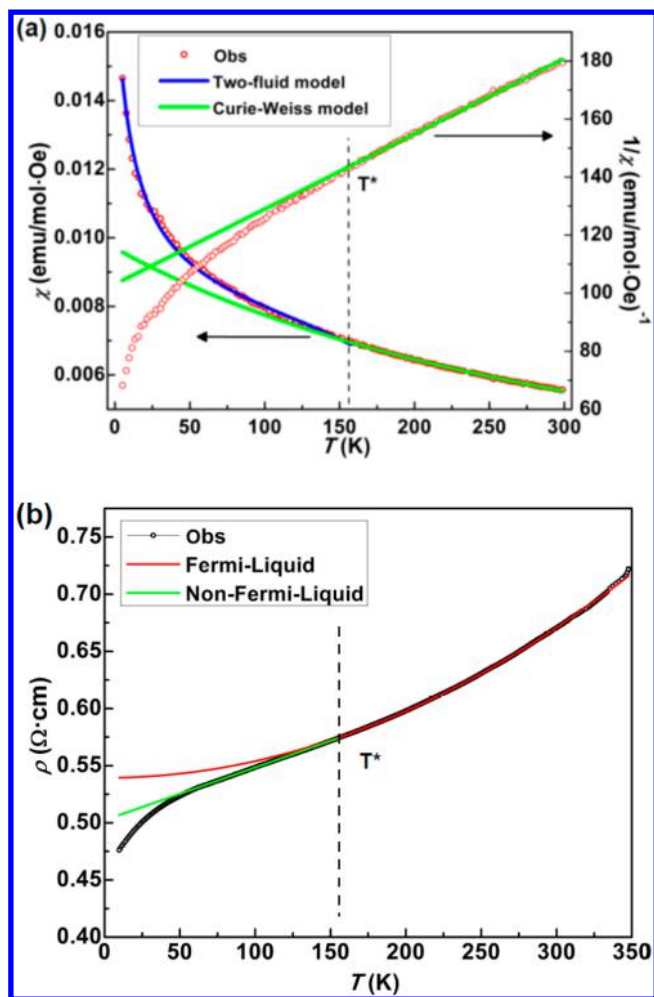


Figure 4. Temperature dependence of (a) magnetic susceptibility $\chi(T)$ and $1/\chi(T)$ measured under $H = 0.1$ T in ZFC procedure, (b) resistivity $\rho(T)$ response of LCIO between 10 and 350 K. The dashed lines show the transition point around the specific temperature $T^* = 155$ K. The temperature T^* separates the two-fluid model and Curie–Weiss fitting, respectively in (a), and non-Fermi-liquid behavior and Fermi-liquid behavior fitting in (b).

types of non-Fermi-liquid behavior: for $58 \text{ K} < T < T^*$, the resistivity fits $\rho(T) = \rho_0 + B \times T$, with $\rho_0 = 0.502 \Omega \cdot \text{cm}$, and $B = 4.62 \times 10^{-4} \Omega \cdot \text{cm} \cdot \text{K}^{-1}$. At the lower temperature regime ($T < 58 \text{ K}$), the resistivity drop suggests heavy-Fermion behavior. To further understand the complex physics of this material, specific heat as well as theoretical calculations were investigated.

3.4. Specific Heat. Figure 5 shows the temperature dependence of specific heat (C_p) on cooling from 400 down to 2 K for LCIO. Figure 5a and its inset are the plots of C_p/T vs T between 2 and 390 K and C_p/T vs T^2 between 2 and 20 K, respectively. In the absence of any anomaly around T^* , the possibility of a second- or first-order structural phase transition at T^* can be ruled out. An anomalous rise below 7 K is notable (Figure 5a). Data between 3.6 and 20 K were fitted by considering three contributions: $C(T) = C_{\text{electron}} + C_{\text{lattice}} + C_{\text{magnetism}}$, where $C_{\text{electron}} = \gamma T$ is the electronic contribution, $C_{\text{lattice}} = \beta T^3$ is the lattice part, and $C_{\text{magnetism}} = \delta T \exp(-T/\Delta)$ is the magnetic contribution. The obtained value of $\gamma = 336 \text{ mJ} \cdot \text{mol}^{-1} \cdot \text{K}^{-2}$ is almost twice as large as that of CCIO, which indicates a much stronger hybridization of Cu 3d and Ir 5d in LCIO. $C_{\text{magnetism}}$ is responsible for the low-temperature rise in

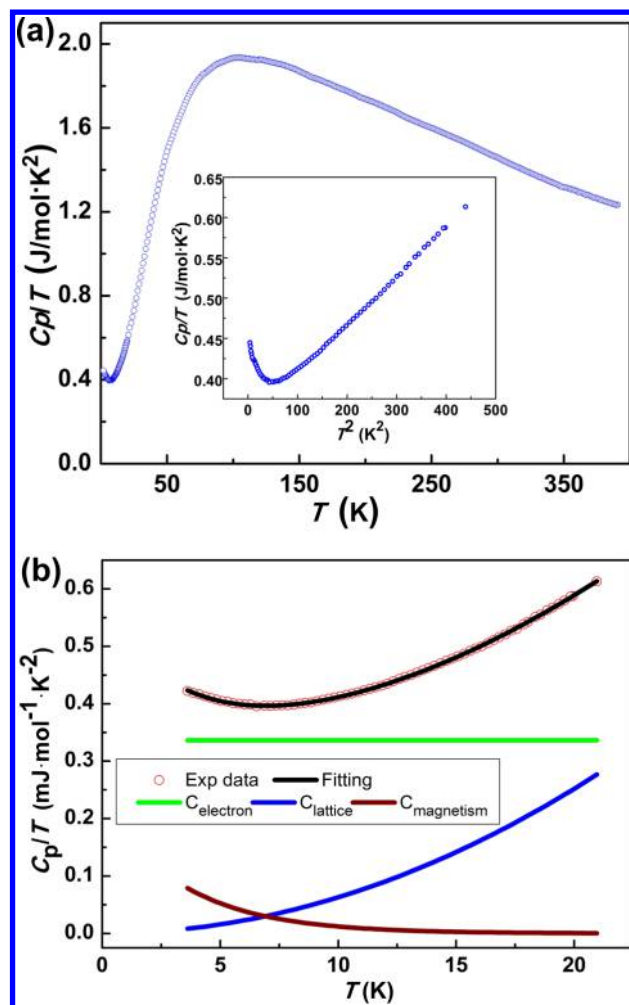


Figure 5. (a) Specific heat $C_p(T)$ and inset showing low-temperature (0–20 K) upturn and the leap of $C_p(T)$ vs T^2 plot. (b) Three parts of specific heat at low-temperature region.

the susceptibility, which suggests that LCIO is close to a magnetic ordering phase or quantum criticality. The Debye temperature $\Theta_D = 395 \text{ K}$ obtained from β ($\beta = 0.629 \text{ mJ} \cdot \text{mol}^{-1} \cdot \text{K}^{-4}$) is very close to that of CCIO ($0.608 \text{ mJ} \cdot \text{mol}^{-1} \cdot \text{K}^{-4}$). The upturn below $\sim 7 \text{ K}$ exhibits no hysteresis (magnetic order change or continuous structural change), future low temperature x-ray and neutron scattering measurements will explore this region in detail. The spin on the magnetic sites is estimated from theoretical DFT simulations as discussed below.

3.5. Theoretical Calculations. The crystal structure of LCIO was calculated theoretically by optimization of the crystal structure of CCIO and replacing Ca by La. The calculated cell volume of LCIO is estimated to increase by $\sim 1.8\%$ compared to that of CCIO due to the differences in ionic sizes (La^{3+} vs Ca^{2+}) and changes of Ir oxidation states ($\text{Ir}^{3.75+}$ vs Ir^{4+}) from calculations,²⁹ which is in good agreement with the observed value ($\sim 2.0\%$) as shown in Table 1. Density of state (DOS, Figure 6 upper panels) from GGA+U calculations indicated a rigid band like shift of DOS between LCIO and CCIO retaining more or less the same basic structures. Note, even though the compound does not order magnetically, in order to describe the correct spin and charge states of the various metal ions of the compound, it is necessary to carry out spin-polarized

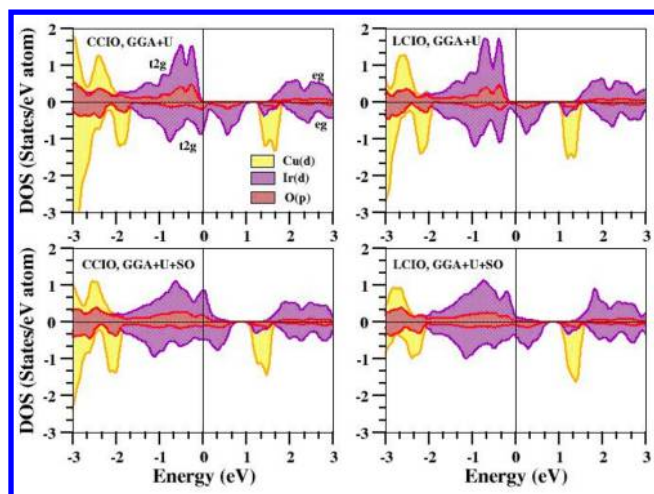


Figure 6. DOS calculated for CCIO (left panels) and LCIO (right panels), projected to Cu *d*, Ir *d*, and O *p* states. Calculations have been carried out within the framework of GGA + U (top panels) and GGA + U + SO (bottom panels) with choice of $U_{\text{Cu}} = 5$ eV, $U_{\text{Ir}} = 2$ eV, and $J_{\text{H}} = 0.8$ eV. The zero of the energy is marked at corresponding Fermi energy.

electronic structure calculation. This gives the correct information concerning the spin and orbit moments of the various components, which is necessary for the meaningful description of the electronic states of the compound. The strong mixing between transition metal *d* states and O *p* states close to the Fermi energy (set as 0 eV) is observed in both LCIO and CCIO. GGA + U treatment leads to half-metallic solutions in both compounds, with finite density of states at the Fermi level for down spin channel and zero density of states at the Fermi level in the up spin channel. Cu appears to be close to Cu^{2+} state with spin split Cu x^2-y^2 states, which makes Ir close to $4+$ in CCIO and $3.75+$ in LCIO, in good agreement with the crystal structure analysis and XANES results.

GGA + U calculations give a magnetic moment (MM) of $0.65 \mu_{\text{B}}$ at the Cu site confirming the close to $2+$ valence (d^9) of Cu. Ir is found to be in a low spin (LS) state, in agreement with general expectation. The calculated MMs at Ir and O sites for LCIO are found to be 0.49 and $0.15 \mu_{\text{B}}$, respectively, which are somewhat smaller than those at Ir and O sites in CCIO ($0.61 \mu_{\text{B}}$ for Ir, $0.19 \mu_{\text{B}}$ for O), because of the filling of Ir–O hybridized state in LCIO. Detailed analysis of the band structure shows that Ir- e_g (σ) states are empty in both spin channels. The Ir- $a_{1g} + e_g$ (π) states are all occupied in the up spin channel, while the Ir- a_{1g} state is partially filled and the Ir- e_g (π) states are occupied in the down spin channel; the Cu xy , xz , yz , $3z^2$ states are found to be all occupied in both spin channels, while the Cu x^2-y^2 state is occupied in the up-spin channel and empty in down-spin channel. This justifies the assignment of the valences. Turning on the spin–orbit, the significant spin–orbit effect at the Ir site mixes the DOS in up and down spin channels. The orbital moment at the Ir site is found to be significant with a value of 0.1 – $0.2 \mu_{\text{B}}$ for both compounds. This destroys the half metallic character of CCIO, making it metallic on both spin channels. The effect is different in the case of LCIO, where half-metallic character is marginally retained. This causes the electronic structure close to the Fermi level to be different between the two compounds, presumably relating to the observation of non-Fermi liquid like behavior in CCIO, and Fermi liquid like in LCIO.

4. CONCLUSION

The second Ir-containing quadruple perovskite $\text{LaCu}_3\text{Ir}_4\text{O}_{12}$ was prepared at high pressure and temperature. It adopts the typical $\text{AA}'_3\text{B}_4\text{O}_{12}$ structure with square planar coordination of Jahn–Teller $\text{A}'\text{--Cu}^{2+}$ cation. Both the magnetism and resistivity of $\text{LaCu}_3\text{Ir}_4\text{O}_{12}$ show different behavior above and below a characteristic temperature ($T^* = 155$ K). The magnetic susceptibility follows the Curie–Weiss Law above T^* but can only be fitted by a two fluid model for heavy-electron materials below T^* , while the resistivity can be fitted to Fermi liquid and non-Fermi liquid behavior above and below T^* , respectively, indicating strong electron hybridization as evidenced by the specific heat data. Compared with the isostructural $\text{CaCu}_3\text{Ir}_4\text{O}_{12}$, the replacement of Ca by La yields a slightly larger unit cell and drives Ir^{4+} (d^5) to mixed-valence state of $\text{Ir}^{3.75+}$ (formally 3Ir^{4+} (d^5) + Ir^{3+} (d^6)) in $\text{LaCu}_3\text{Ir}_4\text{O}_{12}$. First principle calculations are in good agreement with the experimental results and indicate that spin orbit coupling (SOC) destroys the half metallic character of CCIO, making it metallic on both spin channels, while in LCIO the half-metallic character is marginally retained with SOC (Figure 6). Although both $\text{CaCu}_3\text{Ir}_4\text{O}_{12}$ and $\text{LaCu}_3\text{Ir}_4\text{O}_{12}$ are metallic, the La compound is a Fermi liquid above T^* (~ 155 K), while the Ca analogue is a non-Fermi liquid above T^* (~ 80 K), which indicate that electron correlations of the normal state in LCIO and CCIO are fundamentally different. This is corroborated by a very large value of $\gamma = 336 \text{ mJ}\cdot\text{mol}^{-1}\cdot\text{K}^{-2}$, which is almost twice as large as that of CCIO, and indicates a much stronger hybridization of Cu 3d and Ir 5d in LCIO.

The discoveries in $\text{CaCu}_3\text{Ir}_4\text{O}_{12}$ and $\text{LaCu}_3\text{Ir}_4\text{O}_{12}$ suggest an interesting materials design platform, as the chemical potential variation of the A- and A'-site cations can be used to tune the physical properties by inducing valence changes at the B-site Ir in $\text{A}'\text{A}_3\text{Ir}_4\text{O}_{12}$. For example, non-Fermi liquid-to-Fermi liquid transition at higher temperature could be expected in $\text{Ca}_{1-x}\text{La}_x\text{Cu}_3\text{Ir}_4\text{O}_{12}$ ($0 < x < 1$) solid solution at a critical x value, and it is worthy of further exploration. Moreover, a monovalent cation at the A-site of $\text{ACu}_3\text{Ir}_4\text{O}_{12}$ could result in some Ir^{5+} (d^4) at the B-site as in $\text{NaCu}_3\text{Ir}_4\text{O}_{12}$ and $\text{Ca}_{1-x}\text{Na}_x\text{Cu}_3\text{Ir}_4\text{O}_{12}$. Thus, to draw a clear map of the electronic behavior of Ir-perovskite-related compounds, analogous phases should be investigated.

■ ASSOCIATED CONTENT

Supporting Information

The crystallographic information file (CIF). This material is available free of charge via the Internet at <http://pubs.acs.org>.

■ AUTHOR INFORMATION

Corresponding Author

*E-mail: martha@chem.rutgers.edu.

Notes

The authors declare no competing financial interest.

■ ACKNOWLEDGMENTS

This work was supported by the ARO-434603-DOD-VV911NF-12-1-0172 grant. Work at NJIT (T.A.T.) is supported by DOE Grant DE-FG02-07ER46402. The work of J.S.-B. is supported by the Spanish grants MAT2013-41099-R and RyC-2010-06276. The Physical Properties Measurements System used in the heat capacity measurements was acquired under NSF MRI Grant DMR-0923032 (ARPA

award). We thank Ms. J. Hanley at LDEO in Columbia University for making the high pressure assemblies and Dr. F. Mompean for his help in the conductivity measurements.

■ REFERENCES

- (1) Cava, R. J.; Batlogg, B.; van Dover, R. B.; Murphy, D. W.; Sunshine, S.; Siegrist, T.; Remeika, J. P.; Rietman, E. A.; Zahurak, S.; Espinosa, G. P. *Phys. Rev. Lett.* **1987**, *58*, 1676.
- (2) Wang, J.; Neaton, J. B.; Zheng, H.; Nagarajan, V.; Ogale, S. B.; Liu, B.; Viehland, D.; Vaithyanathan, V.; Schlom, D. G.; Waghmare, U. V.; Spaldin, N. A.; Rabe, K. M.; Wuttig, M.; Ramesh, R. *Science* **2003**, *299*, 1719.
- (3) Eerenstein, W.; Mathur, N. D.; Scott, J. F. *Nature* **2006**, *442*, 759.
- (4) de Groot, R. A.; Mueller, F. M.; Engen, P. G. v.; Buschow, K. H. J. *Phys. Rev. Lett.* **1983**, *50*, 2024.
- (5) Zeng, Z.; Greenblatt, M.; Subramanian, M. A.; Croft, M. *Phys. Rev. Lett.* **1999**, *82*, 3164.
- (6) Subramanian, M. A.; Li, D.; Duan, N.; Reisner, B. A.; Sleight, A. W. *J. Solid State Chem.* **2000**, *151*, 323.
- (7) Kobayashi, W.; Terasaki, I.; Takeya, J.-i.; Tsukada, I.; Ando, Y. *J. Phys. Soc. Jpn.* **2004**, *73*, 2373.
- (8) Mezzadri, F.; Calestani, G.; Calicchio, M.; Gilioli, E.; Bolzoni, F.; Cabassi, R.; Marezio, M.; Migliori, A. *Phys. Rev. B* **2009**, *79*, 100106.
- (9) Long, Y. W.; Hayashi, N.; Saito, T.; Azuma, M.; Muranaka, S.; Shimakawa, Y. *Nature* **2009**, *458*, 60.
- (10) Shiro, K.; Yamada, I.; Ikeda, N.; Ohgushi, K.; Mizumaki, M.; Takahashi, R.; Nishiyama, N.; Inoue, T.; Irifune, T. *Inorg. Chem.* **2013**, *52*, 1604.
- (11) Powell, A. V.; Gore, J. G.; Battle, P. D. *J. Alloys Compd.* **1993**, *201*, 73.
- (12) Moon, S. J.; Kim, M. W.; Kim, K. W.; Lee, Y. S.; Kim, J. Y.; Park, J. H.; Kim, B. J.; Oh, S. J.; Nakatsui, S.; Maeno, Y.; Nagai, I.; Ikeda, S. I.; Cao, G.; Noh, T. W. *Phys. Rev. B* **2006**, *74*, 113104.
- (13) Bremholm, M.; Dutton, S. E.; Stephens, P. W.; Cava, R. J. *J. Solid State Chem.* **2011**, *184*, 601.
- (14) Kim, B. J.; Ohsumi, H.; Komesu, T.; Sakai, S.; Morita, T.; Takagi, H.; Arima, T. *Science* **2009**, *323*, 1329.
- (15) Clancy, J. P.; Chen, N.; Kim, C. Y.; Chen, W. F.; Plumb, K. W.; Jeon, B. C.; Noh, T. W.; Kim, Y.-J. *Phys. Rev. B* **2012**, *86*, 195131.
- (16) Xin, Y.; Zhou, H. D.; Cheng, J. G.; Zhou, J. S.; Goodenough, J. B. *Ultramicroscopy* **2013**, *127*, 94.
- (17) Cheng, J. G.; Zhou, J. S.; Yang, Y. F.; Zhou, H. D.; Matsubayashi, K.; Uwatoko, Y.; MacDonald, A.; Goodenough, J. B. *Phys. Rev. Lett.* **2013**, *111*, 176403.
- (18) Walker, D.; Carpenter, M. A.; Hitch, C. M. *Am. Mineral.* **1990**, *75*, 1020.
- (19) Coelho, A. J. *Appl. Crystallogr.* **2000**, *33*, 899.
- (20) Coelho, A. *TOPAS-Academic, General Profile and Structure Analysis Software for Powder Diffraction Data*, version 4.1; Coelho Software: 2007.
- (21) Ravel, B.; Newville, M. *J. Synchrotron Radiat.* **2005**, *12*, 537.
- (22) Hwang, J. S.; Lin, K. J.; Tien, C. *Rev. Sci. Instrum.* **1997**, *68*, 94.
- (23) Blaha, P.; Schwarz, K.; Madsen, G.; Kvasnicka, D.; Luitz, J.; WIEN2k; Technische Universitaet Wien: Austria, 2001.
- (24) Haskel, D.; Fabbri, G.; Zhernenkov, M.; Kong, P. P.; Jin, C. Q.; Cao, G.; van Veenendaal, M. *Phys. Rev. Lett.* **2012**, *109*, 027204.
- (25) Kim, B. J.; Jin, H.; Moon, S. J.; Kim, J. Y.; Park, B. G.; Leem, C. S.; Yu, J.; Noh, T. W.; Kim, C.; Oh, S. J.; Park, J. H.; Durairaj, V.; Cao, G.; Rotenberg, E. *Phys. Rev. Lett.* **2008**, *101*, 076402.
- (26) Laguna-Marco, M. A.; Haskel, D.; Souza-Neto, N.; Lang, J. C.; Krishnamurthy, V. V.; Chikara, S.; Cao, G.; van Veenendaal, M. *Phys. Rev. Lett.* **2010**, *105*, 216407.
- (27) Zhang, S.; Saito, T.; Mizumaki, M.; Shimakawa, Y. *Chem.—Eur. J.* **2014**, *20*, 9510.
- (28) Alonso, J. A.; Sánchez-Benítez, J.; De Andrés, A.; Martínez-Lope, M. J.; Casais, M. T.; Martínez, J. L. *Appl. Phys. Lett.* **2003**, *83*, 2623.
- (29) Shannon, R. *Acta Crystallogr., Sect. A* **1976**, *32*, 751.
- (30) Lufaso, M. W.; Woodward, P. M. *Acta Crystallogr., Sect. B* **2001**, *57*, 725.
- (31) Dezanneau, G.; Audier, M.; Vincent, H.; Meneghini, C.; Djurado, E. *Phys. Rev. B* **2004**, *69*, 014412.
- (32) Sahiner, A.; Croft, M.; Guha, S.; Perez, I.; Zhang, Z.; Greenblatt, M.; Metcalf, P. A.; Jahns, H.; Liang, G. *Phys. Rev. B* **1995**, *51*, 5879.
- (33) Liang, G.; Sahiner, A.; Croft, M.; Xu, W.; Xiang, X. D.; Badresingh, D.; Li, W.; Chen, J.; Peng, J.; Zettl, A.; Lu, F. *Phys. Rev. B* **1993**, *47*, 1029.
- (34) Croft, M.; Sills, D.; Greenblatt, M.; Lee, C.; Cheong, S. W.; Ramanujachary, K. V.; Tran, D. *Phys. Rev. B* **1997**, *55*, 8726.
- (35) Tranquada, J. M.; Heald, S. M.; Moodenbaugh, A. R.; Liang, G.; Croft, M. *Nature* **1989**, *337*, 720.
- (36) Liang, G.; Chen, J.; Croft, M.; Ramanujachary, K. V.; Greenblatt, M.; Hegde, M. *Phys. Rev. B* **1989**, *40*, 2646.
- (37) Li, M.-R.; Walker, D.; Retuerto, M.; Sarkar, T.; Hadermann, J.; Stephens, P. W.; Croft, M.; Ignatov, A.; Grams, C. P.; Hemberger, J.; Nowik, I.; Halasyamani, P. S.; Tran, T. T.; Mukherjee, S.; Dasgupta, T. S.; Greenblatt, M. *Angew. Chem., Int. Ed.* **2013**, *52*, 8406.
- (38) Kayser, P.; Martínez-Lope, M. J.; Alonso, J. A.; Retuerto, M.; Croft, M.; Ignatov, A.; Fernández-Díaz, M. T.; Eur, J. *Inorg. Chem.* **2014**, 178.
- (39) Zuo, J. M.; Kim, M.; O'Keeffe, M.; Spence, J. C. H. *Nature* **1999**, *401*, 49.
- (40) Asbrink, S.; Waskowska, A. *J. Phys.: Condens. Matter* **1991**, *3*, 8173.
- (41) Brese, N. E.; O'Keeffe, M.; Von Dreele, R. B.; Young, V. G., Jr. *J. Solid State Chem.* **1989**, *83*, 1.
- (42) Ryden, W. D. *J. Chem. Phys.* **1970**, *52*, 6058.
- (43) Cao, G.; Bolivar, J.; McCall, S.; Crow, J. E.; Guertin, R. P. *Phys. Rev. B* **1998**, *57*, R11039.
- (44) Yang, Y.-f.; Fisk, Z.; Lee, H.-O.; Thompson, J. D.; Pines, D. *Nature* **2008**, *454*, 611.
- (45) Yang, Y. F.; Pines, D. *Proc. Natl. Acad. Sci. U. S. A.* **2012**, *109*, E3060.